MODE II COHESIVE LAW EXTRAPOLATION PROCEDURE OF COMPOSITE BONDED JOINTS

A. Arrese [1], I. Adarraga[1], N. Insausti [1], J. Renart [2,3], C. Sarrado [2]

[1] *Materials + Technologies Group/ Mechanics of Materials, Faculty of Engineering of Gipuzkoa (UPV/EHU), San Sebastián, Spain*

[2] *AMADE, Polytechnic School (II), University of Girona, Carrer Universitat de Girona , 4, E-17003 Girona, Spain*

[3] *Serra Húnter Fellow, Generalitat de Catalunya, Spain*

Keywords: Adhesive joints; Cohesive law; J-Integral; Mode II, Eccentric-ENF test.

ABSTRACT

A novel extrapolation procedure to predict the mode II cohesive laws of adhesive joints is presented. At first, a recently proposed compliance based experimental method to extract mode II Cohesive Laws is extended to the eccentric end-notched flexure test EENF and generalized including the effect of the bond line thickness and to this end, improved expressions for the compliance, *J*-Integral and shear displacement at the crack tip are derived.

Assuming that every effect associated to the damage is included in the equivalent crack length, new expressions related to the Compliance (C_0), *J*- Integral (J_0) and crack tip shear displacement (Δ_0) are defined and invariant relations between J_0-Δ_0 and Δ_0- C_0 are elicited for a given material system and test configuration.

Finally, an extrapolation procedure is presented, based on the J_0-Δ_0 and Δ_0- C_0 calibrated curves, which enables to estimate the cohesive laws for a wide range of adhesive to adherend ratio of a given material system by processing only the load –displacement curve.

NOMENCLATURE

Latin alphabet

A, A_0	cross sectional area of the specimen and the adherend, respectively
a_t	initial crack tip position
a_{ie}	equivalent initial crack tip position
a_{ie}	equivalent initial crack length
a_e	equivalent crack length
B	regression coefficients of the linear curve J_0-Δ_0
C	compliance
C_0	compliance factor
d	actual span between left support and loading roller
d_0	initial span between left support and loading roller
E_1, E_2, E_3	longitudinal, in-plane and out-of-plane elastic moduli, respectively
E_f	flexural modulus
G_{12}	in-plane shear modulus
G_{13}, G_{23}	out-of-plane shear moduli
g	glue line
$2h$	the total thickness of the specimen
I, I_0	second moment of area of the specimen and the adherend, respectively
J	J-integral value
J_c	J-integral critical value
J_0	J-integral factor
k_p	penalty stiffness
$2L$	actual span between supports
$2L_0$	initial span between supports
m	regression coefficients of the linear curve J_0-Δ_0

M	Bending moment
P	applied load
Q	shear force
R	the support and loading roller radius
t	adhesive thickness
w	specimen width

Greek alphabet

α	shape factor in the deformed configuration
α_0	shape factor in the non deformed configuration
β	adhesive to adherent thickness ratio
χ	specimens cross-sectional factor
δ	load point displacement
Δ_n , Δ_t	opening and shear displacement at the crack tip, respectively
Δ_0	crack tip shear displacement factor
λ_0, λ_1, λ_2	regression coefficients of the quadratic curve Δ_0-C_0
θ_A, θ_B, θ_C	clockwise rotations at the load introduction points
σ	cohesive normal stress
τ	cohesive shear stress
τ_{max}	cohesive shear strength
Ω_1, Ω_2, Ω_3	coefficients of the displacement curve

Acronyms

BTBR	Bending Theory with Bending Rotations
CFRP	Carbon Fiber Reinforced Polymers
CTSD	Crack Tip Shear Displacement
CZM	Cohesive Zone Model
DIC	Digital Image Correlation
DM	Direct Method

EENF Eccentric End Notched Flexure

ENF End Notched Flexure

FPZ Fracture Process Zone

LVDT Linear Variable Differential Transformer

SD standard deviation

1. INTRODUCTION

Adhesive bonding is extensively used in diverse industrial applications [1 2 3 4 -5] allowing a weight reduction and providing design flexibility in structures that require some joining technique. Adhesive bonding offers superior advantages over conventional mechanical fasteners such as higher specific strength, cheaper and faster joining technique, lower stress concentration, and better fatigue resistance. [6 7 -8].

However, due to the lack of reliability that structural joints often suffer [9,10], adhesives have been widely used for reparation and maintenance operations of aeronautic components but the use of adhesive bonding in large primary structural parts is not feasible for the moment [11, 12].

The use of Cohesive Zone Models (CZM) to simulate the failure process of adhesive joints is increasing because of its versatility to analyze the fracture in a wide variety of materials and loading conditions.

CZM, presented by Barenblatt [13] and Dugdale[14], represents a damage zone in the vicinities of the crack tip where the local fracture process is regarded as a gradual phenomenon. CZM relies on a traction separation law, assumed as a constitutive law of the material, which describes the material failure behavior [15].

Adhesive joints are usually affected by a large scale Fracture Process Zone (FPZ) as a result of the size of the plastic and damaged region formed in the vicinities of the crack tip. In this situation, an accurate analysis of the FPZ performance is needed to precisely simulate the joint response [16], an experimental determination of the cohesive law being necessary.

For this aim, there are different methods available in the literature which can be classified into two groups; the inverse and the direct methods.

The inverse procedure consists of a parametric modeling to identify cohesive zone model parameters using the Finite Element Method. This iterative method relies on an optimization procedure which goal is to reach the best compromise between the simulation and the experimental measurements by iteratively varying cohesive zone model variables [17 18 19 20 21 22 23-24].

In the direct methods, the determination of the cohesive law is conducted based on the closed-form expressions of the path independent J-integral to obtain the fracture toughness and by the experimental measurement of the crack tip displacement [23, 25, 26,27 28, 29, 30 ,31, -32] usually requiring high resolution equipments as linear variable differential transformer (LVDT) or Digital Image Correlation (DIC).

In the present study, a recently proposed compliance based experimental method to extract mode II cohesive law [33] is extended for the eccentric end-notched flexure test (EENF) to check the possible advantages of the eccentric test configuration to avoid the influence of the FPZ proximity to the load point position and is generalized to include the effect of the adhesive layer thickness when it is not negligible in comparison with the adherend thickness.

Based on this generalized data reduction method, a new extrapolation procedure to predict the mode II cohesive laws of bonded joints is presented enabling to estimate the mode II cohesive laws for a wide range of adhesive to adherend ratio of a given material system and test configuration by processing only the load-displacement curve.

In **Section 2** novel mathematical expressions for the compliance (C), J-Integral (J) and the crack tip shear displacement (Δ_t) are derived accounting for the eccentricity of the EENF test and the adhesive layer thickness. The determination of J and Δ_t is carried out according to the equivalent crack length approach, for which only the load and displacement data provided by the test machine are required. In **Section 3** new expressions designated as C_0, J_0 and Δ_0 are defined and invariant relations are elicited for a given material system and test configuration, providing an extrapolation procedure to estimate the cohesive laws. Experimental and numerical verifications are presented in **Section 4 and 5** to provide both experimental and numerical evidences of the suitability of the proposed data reduction procedure to extract the cohesive law for different bond configurations. Once verified, the efficiency of the extrapolation procedure and the precision of the extracted cohesive laws are analyzed by comparing predicted cohesive laws with results obtained by the Direct Method (DM) [16]. In **Section 6,** a Monte Carlo

Method based sensitivity analysis is carried out to determine the robustness of the proposed data reduction method. Finally, in **Section 7** summary and conclusions are presented.

2. ANALYTIC APPROACH

By evaluating the path independent *J*-integral introduced by Rice [34] locally around the cohesive zone, the *J*-integral becomes [25]:

$$J = \int_0^{\Delta_n} \sigma \, d\Delta_n + \int_0^{\Delta_t} \tau \, d\Delta_t \tag{1}$$

where σ and τ the cohesive normal and shear stress and Δ_n and Δ_t are the opening and shear displacement at the crack tip, respectively.

For the Eccentric End Notched Flexure (EENF) test configuration in Fig. 1, where a specimen cracked at one end is loaded in eccentric three point bending, the cohesive shear stress τ is only function of the crack tip shear displacement Δ_t [35]:

$$\tau(\Delta_t) = \frac{\partial J}{\partial \Delta_t} \tag{2}$$

According to Eq (2) the determination of the cohesive shear stress distribution requires the monitorization of the *J*-Integral versus Δ_t during the EENF test.

For this purpose, a recently proposed experimental method [33] is further developed to account for the influence of adhesive layer thickness when it is not negligible in comparison with the adherend thickness and extended to include the effect of the eccentricity of the EENF.

This method is a compliance based data reduction method that enables to determine both the *J* and Δ_t using exclusively the load displacement data recorded during the test without any external measurement of the crack length and the displacement at the crack tip and including in addition to the span variation, shear and local deformation effects, the influence of thickness of the adhesive layer.

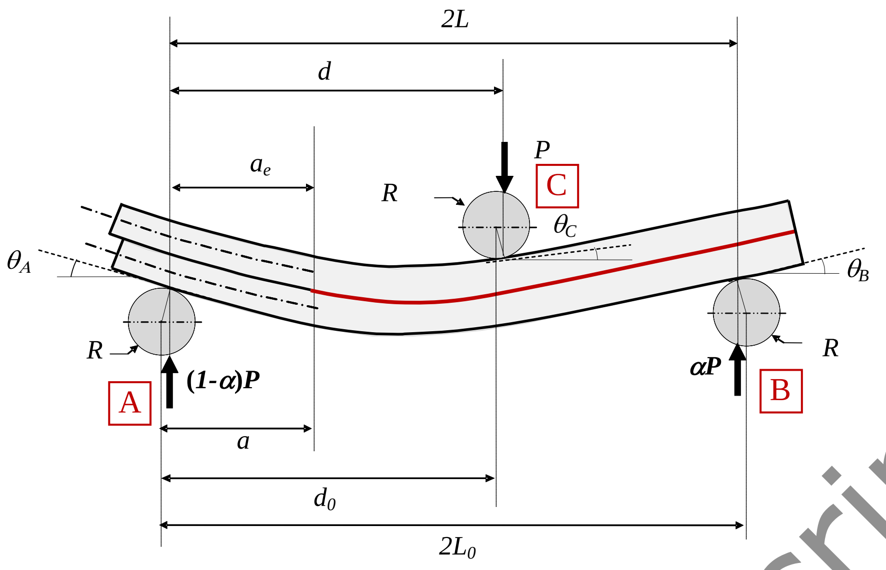

Figure 1: Schematic EENF specimen according to BTBR

2.1. Equivalent Crack Length

To obtain the equivalent crack length based on the compliance of the specimen, elastic behavior of the adherends is assumed during the whole fracture test process.

The load application point displacement is determined applying Castigliano's second theorem [36] including shear and bending effects and obtaining the derivatives of shear forces and bending moments by the unit load method. Thus, the compliance $C = \delta/P$ can be expressed as:

$$C = \frac{12(1-\alpha)^2}{E_f w(2h)^3}\left[\frac{1}{\chi}\frac{{a_e}^3}{3} + \alpha^2\frac{(2L)^3}{3}\right] + \frac{6}{5}\frac{(1-\alpha)}{G_{13}w(2h)}\left[(1-\alpha)\left[\frac{\beta}{1-\beta}\right]a_e + \alpha(2L)\right] \tag{3}$$

Where a_e is the equivalent crack length, E_f is the flexural modulus; G_{13} is out-of-plane shear modulus, $\alpha = d/2L$ is the shape factor accounting for the eccentricity of the EENF test in the deformed configuration, w the width and $\beta = t/2h$ adhesive to adherent thickness ratio, where t adhesive thickness and $2h$ the total thickness of the specimen. Further details of the derivation of Eq (3) are provided in Appendix A.

The χ factor can be computed as:

$$\chi = \frac{(1-\beta)^3}{4-(1-\beta)^3} \tag{4}$$

The actual span between supports *2L* and the actual span between left support and loading roller *d* (Fig. 1), are determined taken into account the contact point shifting between the specimen and supports and loading rollers due to bending rotation [37]. According to Fig. 1, *2L* and *d* are respectively:

$$2L = 2L_0\left[1 - \frac{R}{2L_0}(|\theta_A| + |\theta_B|)\right] \qquad d = \alpha(2L) = d_0\left[1 - \frac{R}{d_0}(|\theta_A| - |\theta_C|)\right] \tag{5}$$

where $2L_0$ the initial span between supports, d_0 is the initial distance between left support and loading roller and *R* the support and loading roller radius.

In order to evaluate the actual dimensions, the rotations at supports and loading point are determined applying Castigliano's second theorem, being the derivatives obtained applying a unit bending moment at the point where the rotation is going to be determined. The bending rotations are:

$$\begin{aligned}
|\theta_A| &= (1-\alpha)P\left[\frac{12}{E_f w(2h)^3}\left[\frac{1}{\chi}\left(\frac{{a_e}^2}{2} - \frac{{a_e}^3}{3(2L)}\right) + \frac{\alpha(2-\alpha)(2L)^2}{6}\right] + \frac{6}{5G_{13}w(2h)}\left[\frac{\beta}{1-\beta}\right]\left[\frac{a_e}{(2L)}\right]\right] \\
|\theta_B| &= (1-\alpha)P\left[\frac{12}{E_f w(2h)^3}\left[\frac{1}{\chi}\frac{{a_e}^3}{3(2L)} + \frac{\alpha(1+\alpha)(2L)^2}{6}\right] - \frac{6}{5G_{13}w(2h)}\left[\frac{\beta}{1-\beta}\right]\left[\frac{a_e}{(2L)}\right]\right] \\
|\theta_C| &= (1-\alpha)P\left[\frac{12}{E_f w(2h)^3}\left[\frac{1}{\chi}\frac{{a_e}^3}{3(2L)} - \frac{\alpha(1-2\alpha)(2L)^2}{3}\right] - \frac{6}{5G_{13}w(2h)}\left[\frac{\beta}{1-\beta}\right]\left[\frac{a_e}{(2L)}\right]\right]
\end{aligned} \tag{6}$$

Thus, replacing the corrected dimensions from Eq. (5) into Eq (3), the equivalent crack length a_e is determined through a numerical solution equating Eq. (3) to the experimental compliance value obtained directly from the experimental load displacement curve. Based on the compliance variation of the specimen as damage develops, a_e can be estimated at any stage of the test where *P* and δ are evaluated.

2.2. J- Integral

J is determined using the *J*-integral closed form expression for the EENF test presented by Stigh et al. [30].

$$J = \frac{P}{w}[(1-\alpha)\theta_A - \theta_C + \alpha\theta_B] \tag{7}$$

where θ_A, θ_B, and θ_C are the clockwise rotations at the load introduction points and α is the shape factor accounting for the eccentricity of the EENF test in the deformed configuration. Replacing bending rotations θ_A, θ_B, and θ_C obtained from Eq. (6) into Eq. (7) J can be computed as:

$$J = \frac{6P^2(1-\alpha)^2}{E_f w^2 (2h)^3}\left[\frac{{a_e}^2}{\chi}\right] \tag{8}$$

Replacing the corrected dimensions from Eq. (5) and the equivalent crack length determined by Eq. (3) into Eq. (8), J is determined, obtaining the evolution of J during the test exclusively from experimental load-displacement data.

2.3. Crack Tip Shear Displacement

According to previous works [33, 38], every effect associated with the development of the FPZ, is included in the equivalent crack length as displayed in Fig 2.

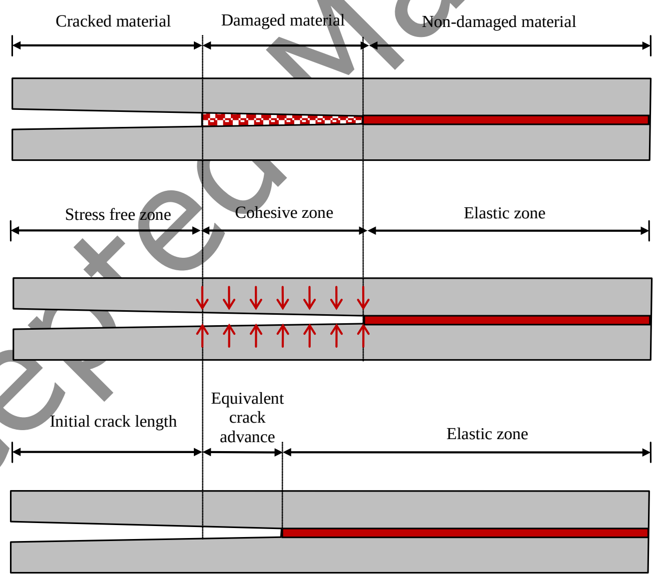

Figure 2: FPZ of an adhesive joint (a) CZM idea (b) and the equivalent crack length based system (c).

Therefore, the shear displacement at the initial crack tip position Δ_t is obtained based on the hypothesis of the equivalent crack length system as shown in Fig 3. Where the black lines represent the cross sectional rotation of the upper and lower arm at the initial crack tip position. The CTSD is the distance/jump between those two lines after removal the rigid body rotation.

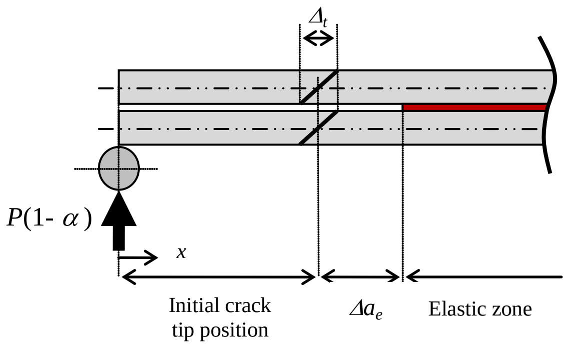

Figure 3: Initial crack tip shear displacement, where Δa_e is equivalent crack advance.

Applying Castigliano's second theorem, and a pair of unit forces in opposite directions at the initial crack tip to obtain the derivatives, the Δ_t can be expressed as

$$\Delta_t = \frac{12P(1-\alpha)(1+\beta)}{E_f w(2h)^2(1-\beta)^3}\left[{a_e}^2 - {a_{te}}^2\right] \tag{9}$$

with

$$a_{te} = a_i\left[1 - \frac{R}{a_t}|\theta_A|\right] \tag{10}$$

where a_t the initial crack tip position, R the radius of the supports roller, $\alpha = d/2L$ the shape factor in the deformed configuration and θ_A the rotation at the left support determined according to Eq. (6) where the corrected dimensions and the effect of the adhesive layer thickness are included.

3. COHESIVE LAW EXTRAPOLATION PROCEDURE

In the following section, a methodology to extrapolate the cohesive law for a given material system and test configuration is presented.

In previous section a method for extracting the mode II cohesive law including bondline thickness effect has been proposed. The method based on beam theory assumes that every effect associated to the damage development is included in the equivalent crack length obtained based on the compliance variation.

Analytical expression for the Compliance, the CTSD and *J*-Integral have been derived, all of them function of the adherends elastic properties (E_f and G_{13}), the test configuration (*R*, *d*, and *2L*), the specimens cross-sectional dimensions (*2h*, *t* and *w*), the applied load (*P*) and the equivalent crack length (a_e).

To be able to rearrange the Compliance, the CTSD and *J*-Integral expressions in a separable form as a multiplication of separate functions, it is necessary to define C-C_{ini} whose expression has the following simplified form according to Eq (A10):

$$C - C_{ini} = \left[\frac{1}{w(2h)^3\chi}\right]\left[\frac{4(1-\alpha)^2}{E_f}\right]\left[\; {a_e}^3 - {a_{ie}}^3\right] \qquad (11)$$

where the first term is related to cross-sectional dimensions, the second term to the elastic properties of the adherends and the test configuration and finally the last term to the equivalent crack length.

Rewriting both Eq (8) and Eq (9) in a separable form, they can be expressed as:

$$J = [P^2]\left[\frac{1}{w^2(2h)^3\chi}\right]\left[\frac{6(1-\alpha)^2}{E_f}\right]\left[{a_e}^2\right] \qquad (12)$$

$$\Delta_{\mathrm{t}} = [P]\left[\frac{(1+\beta)}{w(2h)^2(1-\beta)^3}\right]\left[\frac{12(1-\alpha)}{E_f}\right]\left[{a_e}^2 - {a_{te}}^2\right] \qquad (13)$$

For a given material system (E_f and G_{13}) and test configuration (*R*, *d*, and *2L*), factoring out of C-C_{ini} , J and Δ_{t} in Eq. (11), Eq. (12) and Eq. (13) respectively, the term related to the cross sectional dimensions and the applied load the following C_0, J_0 and Δ_0 functions are defined:

$$\begin{aligned}
(C - C_{ini}) &= \left[\frac{1}{w(2h)^3\chi}\right] \boldsymbol{C}_0(a_e) &\longrightarrow\quad \boldsymbol{C}_0(a_e) &= \frac{4(1-\alpha_0)^2}{E_f}\left[{a_e}^3 - {a_{ie}}^3\right] \\
J &= [P^2]\left[\frac{1}{w^2(2h)^3\chi}\right] \boldsymbol{J}_0(a_e) &\longrightarrow\quad \boldsymbol{J}_0(a_e) &= \frac{6(1-\alpha_0)^2}{E_f}{a_e}^2 \\
\Delta_t &= [P]\left[\frac{(1+\beta)}{w(2h)^2(1-\beta)^3}\right] \boldsymbol{\Delta}_0(a_e) &\longrightarrow\quad \boldsymbol{\Delta}_0(a_e) &= \frac{12(1-\alpha_0)}{E_f}\left[{a_e}^2 - {a_{te}}^2\right]
\end{aligned} \qquad (14)$$

where it is assumed that the effect of span reduction due to contact point shifting affects similarly to all the specimens for a given test configuration $\alpha = \alpha_0 = d_0/(2L_0)$.

According to the polynomial expressions of J_0 and Δ_0 with respect to a_e, Eq (14) suggests that the J_0-Δ_0 follows a linear relationship:

$$\boldsymbol{J_0} = m\,\boldsymbol{\Delta_0} + B \tag{15}$$

where m and B are regression coefficients determined from least squares fitting, that according Eq (14) can be obtained as:

$$m = \frac{(1-\alpha_0)}{2} \qquad B = \frac{6(1-\alpha_0)^2}{E_f}\,{a_{te}}^2 \tag{16}$$

On the other hand, Eq (14) also suggests that Δ_0-C_0 can be fitted to a second order polynomial derived from a Maclaurin series expansion of a function type of $(x+a)^{2/3}$:

$$\boldsymbol{\Delta_0} = \lambda_2 {\boldsymbol{C}_0}^2 + \lambda_1 \boldsymbol{C}_0 + \lambda_0 \tag{17}$$

where λ_2, λ_1 and λ_0 are regression coefficients and have the following form:

$$\lambda_0 = \frac{12(1-\alpha_0)}{E_f}\left({a_{ie}}^2 - {a_{te}}^2\right) \qquad \lambda_1 = \frac{2}{(1-\alpha_0)a_{ie}} \qquad \lambda_2 = -\frac{E_f}{12(1-\alpha_0)^3\ a_{ie}^4} \tag{18}$$

According to Eq (14-18), all regression coefficients depend solely on the material properties and the test configuration and do not depend on cross sectional dimensions, hence it can be set that the J_0-Δ_0 and Δ_0-C_0 curves are unique/ invariant for a given material system and test configuration i.e. the invariant nature of the J_0-Δ_0 and Δ_0-C_0 curves allows considering these curves as a property of the material system and test configuration. This fact leads to the following interesting result:

If J_0-Δ_0 and Δ_0-C_0 curves are calibrated for a given material system and test configuration, then it would be possible to extrapolate the J and Δt and consequently the cohesive law for different adherend and adhesive thicknesses of the same material system and test configuration by monitoring only the load-displacement curve.

3.1. Calibration of J_0-Δ_0 and Δ_0-C_0 curves

The starting point of the calibration procedure is the simultaneous record of load versus loading point displacement, J- integral and CTSD of a single specimen test.

Initially each value of C-C_{ini}, CTSD and J -Integral corresponding to each experimental record are factorized where i refers to the ith loading point as shown in Fig 4. Thereafter, thought the functions expressed in Eq (15) and Eq (17) the factorized data can be fitted determining the regression constants m, B, λ_2, λ_1 and λ_0.

Thus, following the flow diagram shown in fig 4, the J_0-Δ_0 and Δ_0-C_0 curves can be calibrated using a single specimen test data.

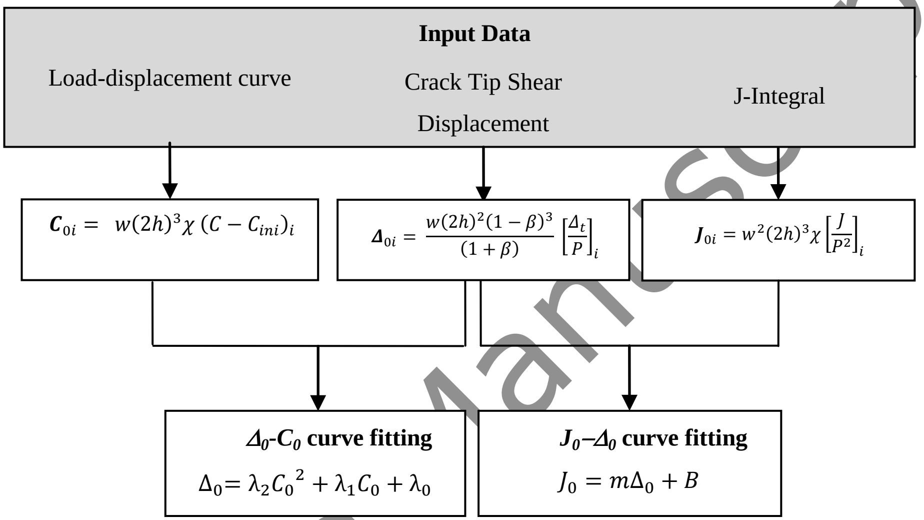

Figure 4. Flow diagram of J_0-Δ_0 and Δ_0-C_0 curve extraction.

3.2. Extrapolation procedure

Once calibrated the J_0-Δ_0 and Δ_0-C_0 curves for a given material system and test configuration, the J- integral and CTSD can be evaluated at all the loading points for other specimens of the same material system and test configuration varying the adhesive and adherent thicknesses by processing only the load-displacement curve.

The extrapolation procedure is shown in the flow diagram in Fig (5).

Initially each value of C-C_{ini} corresponding to each experimental record is factorized where i refer to the ith loading point. According to the Δ_0-C_0 curve a Δ_{0i} value corresponding to each C_{0i} value can be obtained, and consequently using the J_0-Δ_0 curve a J_{0i} value corresponding to each $\Delta_{0i.}$. Knowing the values of Δ_{0i} and J_{0i} for each ith loading point, the J-integral versus CTSD curve is obtained by Eq (14) and according to Eq (2) the corresponding cohesive law by numerical differentiation.

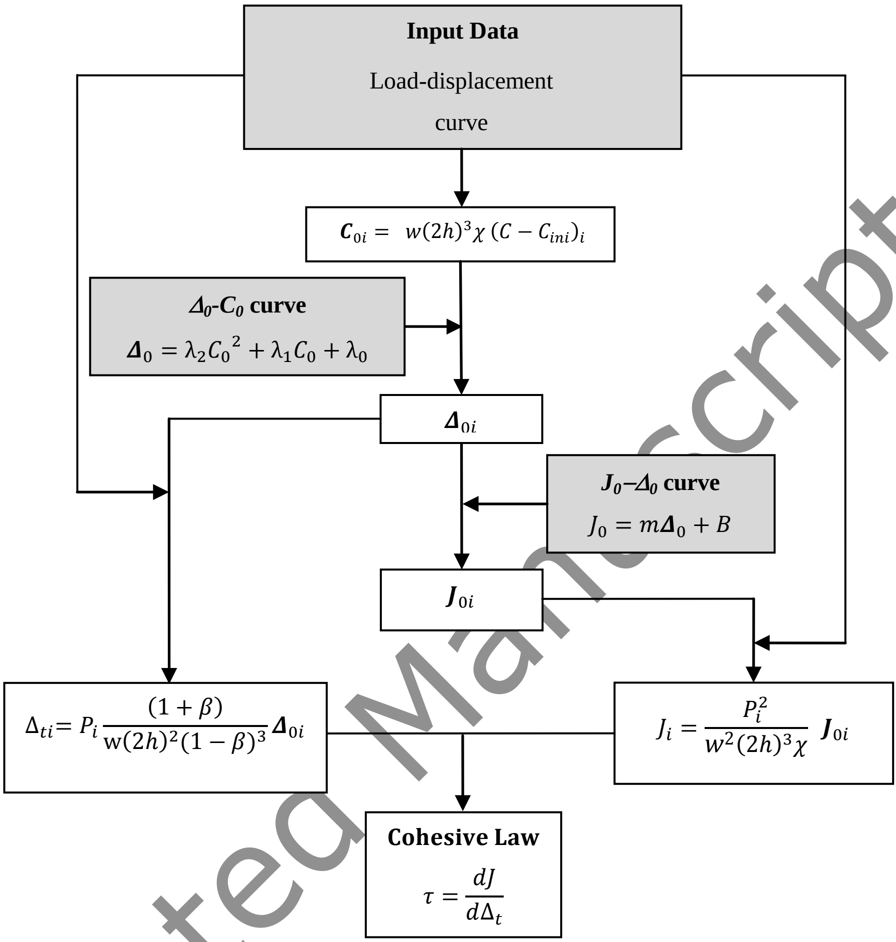

Figure 5. Flow diagram to extrapolate the Cohesive Law.

The extrapolation procedure presented above permits determining the cohesive law for a given material system varying the adhesive and adherent thicknesses by processing only the load-displacement curve, calibrating previously the J_0-Δ_0 and Δ_0-C_0 curves using a single specimen test data.

4. VERIFICATION OF THE PROPOSED METHOD

4.1. Numerical

A two dimensional finite element analysis (FEA) was conducted to examine the suitability of the proposed data reduction procedure to extract the cohesive law for different EENF test configurations, and on the way, to check the advantages of the eccentric test configuration due to the wider path length for the development of the fracture process zone ensuring the stable propagation of the crack [39].

In the considered EENF specimen configuration the support span is *2L* = 120 mm; the width is *w*= 25 mm, the total thickness *2h*=3.2 mm; the adhesive thickness t= 0.2mm and the elastic properties corresponding to the adherends and the adhesive are shown on Table 1.

Table 1. Properties of T800S/M21 UD [40, 41] adherend and FM-300M [42] adhesive

E_{11}	134.7 GPa	G_{adh}	1016MPa
$E_{22}=E_{33}$	7.7 GPa	τ_{max}	47.5MPa
$G_{12}=G_{13}$	4.2 GPa	J_{II}	7.9N/mm
G_{23}	2.8 GPa		
$\nu_{12}=\nu_{13}$	0.34		
ν_{23}	0.4		

The model was developed in ABAQUS using four-node 2D plane strain elements (CPE4) for the adherends and finite thickness four-node cohesive elements (COH2D4) to model the adhesive fracture behavior. Concerning the mesh size, 0.2-mm-long cohesive elements were used to ensure enough elements within the FPZ and the thickness of the cohesive elements was that of the adhesive layer. Regarding the adherends, 0.2-mm-long 8 elements through the thickness were used. The effect of loading and supporting rollers has not been taken into account in the model.

Three test configurations were compared varying the location of the loading point to α=0.5 (corresponding to an ENF test), α=0.6 and α=0.7. The fracture behavior of the adhesive layer was modeled by the input cohesive laws shown in Table 2 with an initial penalty stiffness of $K_p = \frac{G_{adh}}{t} = 5080 N/mm^3$ [42].

The following input cohesive laws have been used:

Table 2. Cohesive laws used in the finite element analyses.

Bilinear			Tabular with a exponential Softening		
J_c (N/mm)	τ_{max} (MPa)	k_p (N/mm^3)	J_c (N/mm)	τ_{max} (MPa)	k_p (N/mm^3)
7.9	47.5	5080	7.9	47.5	5080

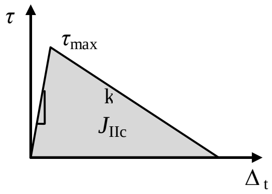

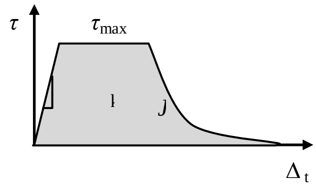

The initial crack length was set to 42 mm for the ENF configuration, to 47 mm for the EENF (α=0,6) configuration and to 52 mm for the EENF (α=0,7) configuration in order to ensure a stable propagation according to [39], being the minimum value of the initial crack length determined by $a_{min} = 2L_0\sqrt[3]{\frac{1}{6}\left(\frac{d_0}{2L_0}\right)^2}$.

4.2. Experimental

T800S/M21 carbon/epoxy unidirectional prepreg were used to manufacture the specimens. The CFRP laminates were manufactured in advance and then secondary bonded using FM-300 epoxy adhesive film. Each specimen was prepared with an initial 60mm long crack by using a teflon insert.

Concerning specimen dimensions the length was 250 mm and the width w=25 mm for all of them. The different adherend and adhesive thicknesses tested are shown in Table 3. The support and loading roller diameters of the test setup are $2R$ = 9.95 mm. The elastic properties of the adherends are E_{11}=134.7GPa, E_{22}= E_{33}=7.7GPa and G_{12}=G_{13}= 4.2GPa [40].

Table 3. Specimen configurations being g the position of the insert [16]

Specimen	$2h$ (mm)	Layup	t (mm)
A1T1	3.12 ± 0.06	$[0]_8 / g / [0]_8$	0.21 ± 0.02
A2T1	4.60 ± 0.08	$[0]_{12} / g / [0]_{12}$	0.21 ± 0.02
A2T2	4.80 ± 0.10	$[0]_{12} / g / [0]_{12}$	0.37 ± 0.01
A3T1	6.05 ± 0.23	$[0]_{16} / g / [0]_{16}$	0.21 ± 0.02

ENF tests were carried out based on AITM 1.0006 [43], being $d_0=L_0$. All the tests were carried out for a support span of $2L_0$=120 mm and an initial crack length of 35 mm to have sufficient space for the full development of the FPZ before the damaged zone reaches the loading point of the specimen.

The ENF tests were run under displacement control in a servohydraulic MTS 858 testing machine using a 5 kN load cell. The displacement rate was varied from 0.5 mm/min to 2.0mm/min according to [43] in order to get a constant strain rate for each specimen thickness and low enough to ensure quasi-static crack growth. A load cell of 5 kN was used to measure the load and the displacement refers to the crosshead displacement of the testing machine. The specimens were painted with a random black on white speckle pattern in one edge to measure the displacement at the crack tip using a Digital Image Correlation (DIC) system. Three inclinometers were installed at load introduction points (points A, B and C in Fig. 1). The synchronization of all systems was carried out by using a common displacement channel.

4.3. Data reduction Methods

The cohesive laws were obtained by the three different data reduction schemes compared in this work: the Direct Method, the BTBR method and extrapolation procedure.

1) **Direct method (DM)** [16]**:** J is obtained substituting into Eq. (7) the measured rotations at loading introduction points and the α = 1/2 shape factor. The crack tip shear displacement is monitored by DIC system at the initial crack tip. Finally, the cohesive law is determined by numerical differentiation according to Eq (2). It is assumed that the monitoring of rotations and displacement is performed while the FPZ is being developed [44].
2) **BTBR method**: The load-displacement curve is registered and J is determined replacing in Eq (8) the equivalent crack length determined by Eq (3) and the corrected dimension obtained in Eq. (5). The crack tip shear displacement Δ_t is determined from Eq (9). Finally, to avoid excessive noise of experimental data, relation J- Δ_t is written as a logistic function [23, 38] and the cohesive law is determined according to Eq (2).

3) **Extrapolation procedure:**

a. **Calibration:** The J_0-Δ_0 and Δ_0-C_0 curves are calibrated according to the flow chart presented in Fig 4.

b. **Extrapolation.** The J and Δ_t for each specimen can be extrapolated according the flow diagram shown in Fig 5. Finally, the cohesive law is obtained according to Eq (2).

The input requirements of the different methods compared in this work are shown in Table 3. It must be noticed that in the present study, the input data used in the calibration procedure (J and Δ_t) is obtained by the BTBR method.

Table 4. Inputs required by the data reduction schemes compared in this work: Direct Method, BTBR method and the Extrapolation procedure.

	Direct Method	**BTBR**	**Extrapolation Procedure**	
			Calibration	**Extrapolation**
Dimensions	w	$w, 2h, t, d_0, 2L_0$	$w, 2h, t, d_0, 2L_0$	$w, 2h, t$
Elastic Properties	None	E_f and G_{13}	E_f and G_{13}	None
Measurements during the test	$P, \theta_A, \theta_B, \theta_C, \Delta_t$	P and δ	P and δ	P and δ

5. RESULTS

5.1. Numerical Results

Fig. 6 shows the load displacement curves corresponding to the three tested configurations. As it can be seen, in the ENF test, the load reaches a maximum value and it remains practically constant, while in the case of the eccentric configurations, the load reaches a maximum value and subsequently drops while the displacement progresses.

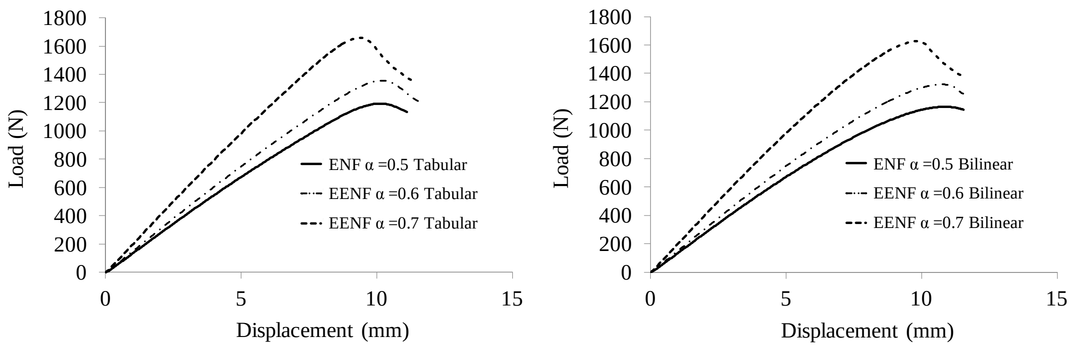

Figure 6. Load displacement curves for the ENF α=0.5, EENF α=0.6 and EENF α=0.7 tests, respectively for the tabular input cohesive law on the left and the bilinear input cohesive law on the right.

Fig. 7 shows the stress profile along the crack path in ENF α=0.5, EENF α=0.6 and EENF α=0.7 tests for the tabular (left) and bilinear (right) input cohesive laws. The stress distribution ahead of the crack tip corresponding to the ENF test, shown in **Fig. 7a**, reveals that the plateau response of the load displacement curve can be due to the proximity of the fracture process zone to the local compression at load application point, hindering the development of the FPZ. According to **Fig. 7b** and **Fig. 7c**, changing the load application point to α=0.6 and α=0.7, ensuring the stable crack propagation requirements with the initial crack length, provides a wider path to fully develop the fracture process zone, without preparing any special equipment or specimen.

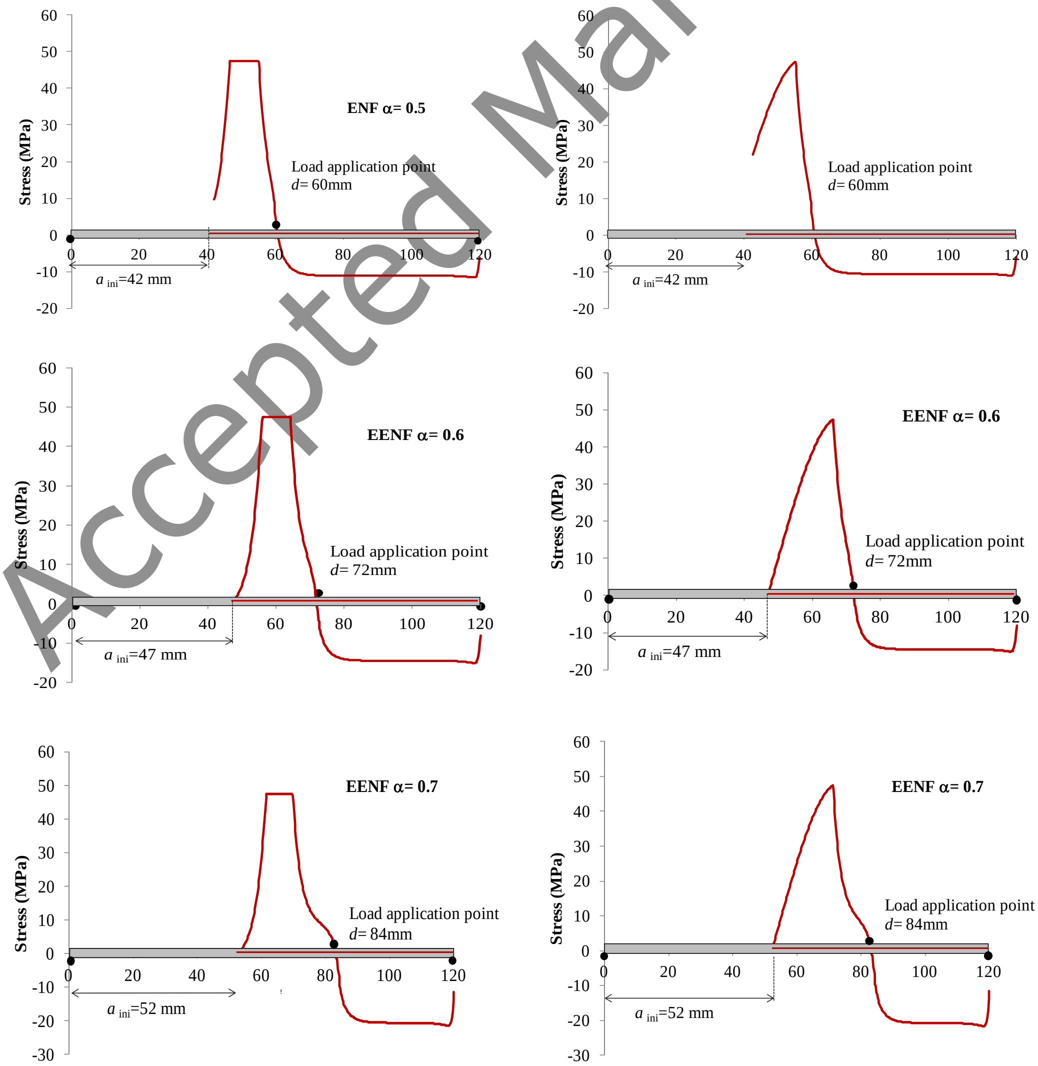

Figure 7. Stress distribution along the (a) ENF, (b) EENF0.6 and (c) EENF0.7 specimens, respectively for the tabular input cohesive law on the left and the bilinear input cohesive law on the right.

Is worth noting that the eccentricity of the load application increases the shear stress in the untracked region, to ensure that the untracked region remains elastic it is verified that the shear stress does not exceed τ_{max} = 47.5 MPa for all the analyzed cases. It is also ensured that the maximum adherend bending stresses not exceed the longitudinal compressive strength of T800S/M21 UD [45].

Applying the generalized BTBR to the load-displacements curves obtained for each virtual test shown in **Fig 6**, results in **Fig 8** show that the generalized BTBR method works properly for the eccentric ENF test configurations and that is sensitive enough to detect the problems on the full development of the fracture process zone observed in the current ENF test.

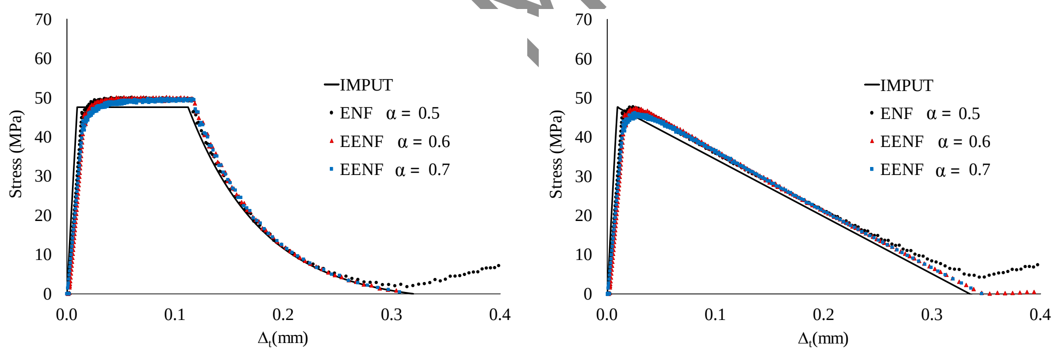

Figure 8. Cohesive laws for ENF, EENF 0.6 and EENF 0.7 specimens, respectively for the tabular input cohesive law on the left and the bilinear input cohesive law on the right..

5.2. Experimental Results

The results of seven ENF experimental tests performed are presented, corresponding to two A1T1 specimens, two A2T2 specimens, two A2T1 specimens and one A3T1 specimen.

Four different specimen configurations have been tested combining two adhesive thicknesses and three adherend thicknesses obtaining different Experimental Load-Displacement responses aiming to demonstrate the suitability of the proposed methods in a wide range of specimen configurations.

The experimental load displacement curves are presented in **Fig. 9.**

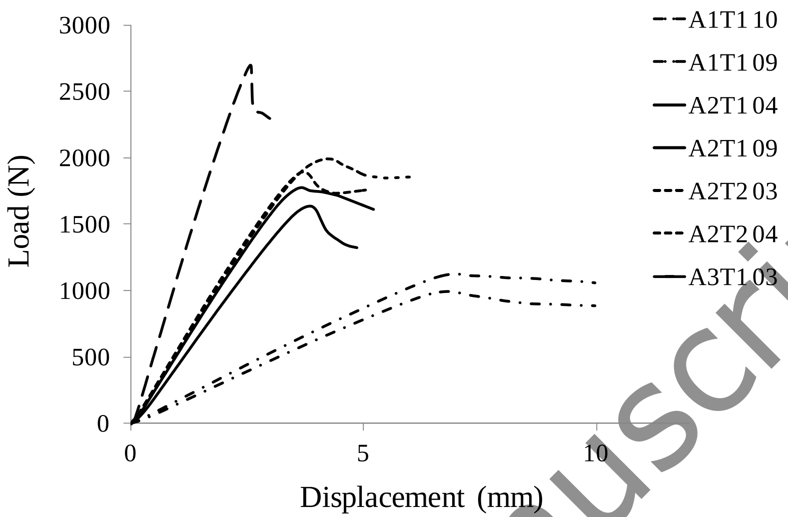

Figure 9: Experimental Load-Displacement curves [16].

5.2.1. Direct method vs. BTBR method

First of all, the *J-Δ* curves and the cohesive laws determined by the generalized BTBR and DM are compared in **Figs. 10-16** to verify the precision of the proposed new model. Results neglecting the thickness of the cohesive layer are also included, to evaluate the need of including the effect of the thickness of the adhesive layer in the model for the correct prediction of the cohesive law.

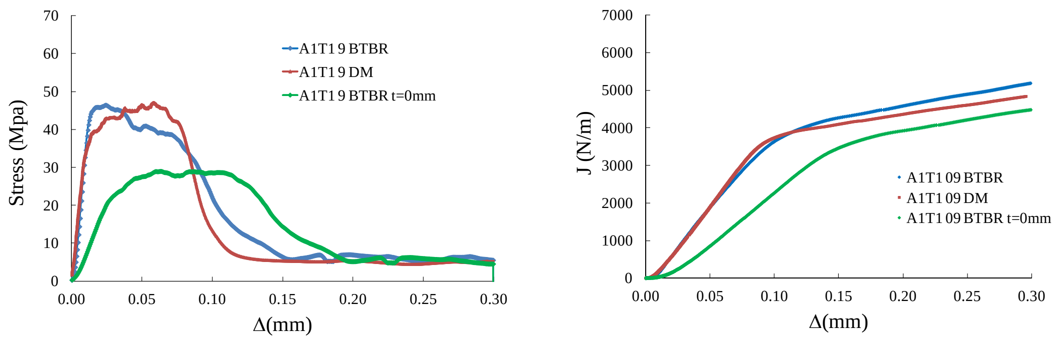

Figure 10: J-Δ_t curves and Cohesive Laws for the tested specimen A1T1 09

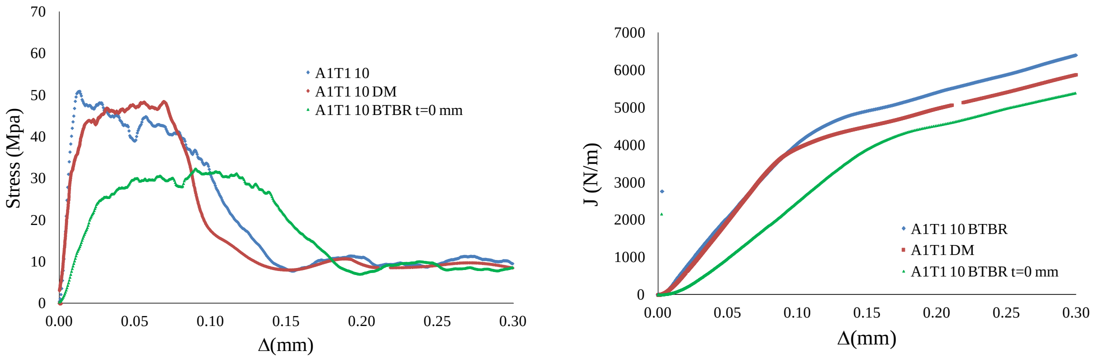

Figure 11: J-Δ_t curves and Cohesive Laws for the tested specimen A1T1 10

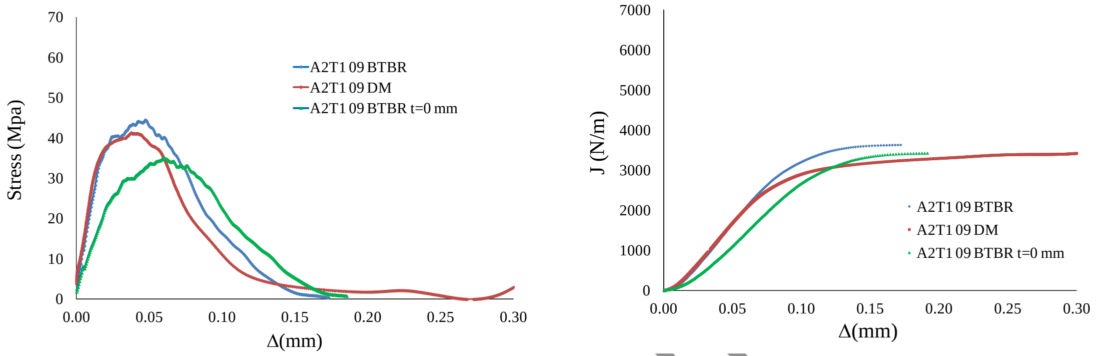

Figure 12: J-Δ_t curves and Cohesive Laws for the tested specimen A2T1 09

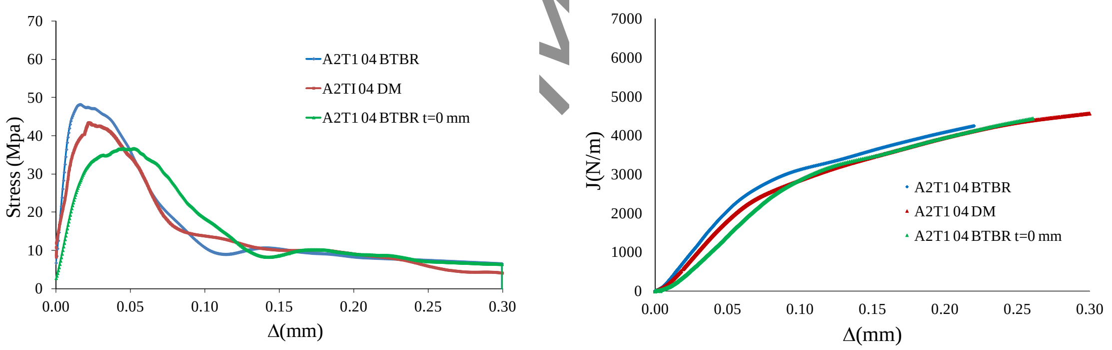

Figure 13: J-Δ_t curves and Cohesive Laws for the tested specimen A2T1 04

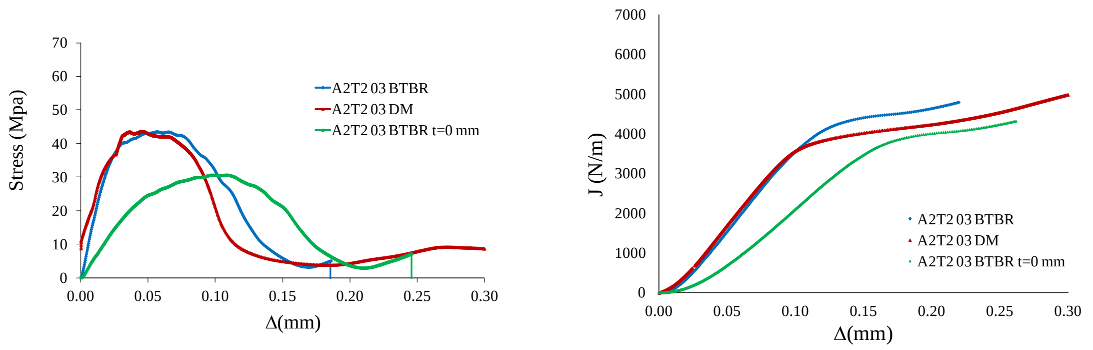

Figure 14: J-Δ_t curves and Cohesive Laws for the tested specimen A2T2 03

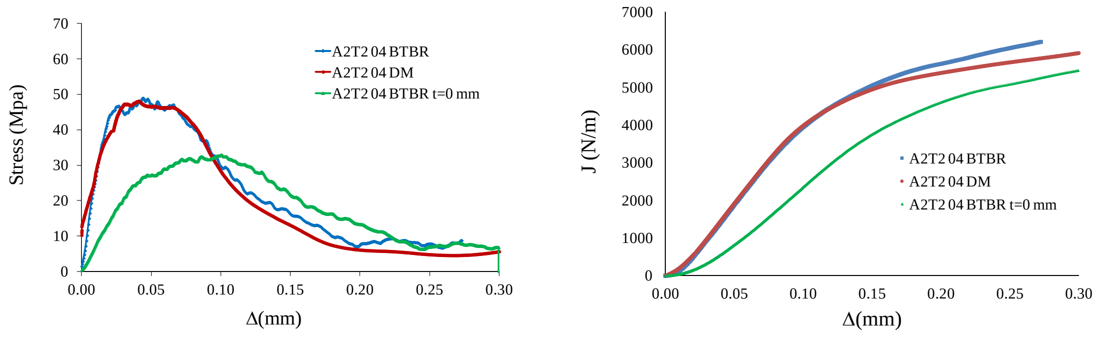

Figure 15: *J*-Δ_t curves and Cohesive Laws for the tested specimen A2T2 04

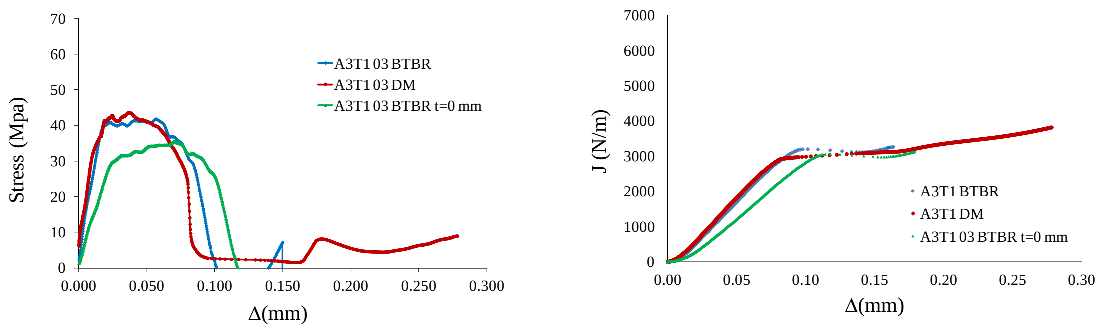

Figure 16: *J*-Δ_t curves and Cohesive Laws for the tested specimen A3T1

According to **Figs. 10-16**, the generalized BTBR method can predict both the form and the maximum stress corresponding to each of the tested configurations accurately; being the results obtained by the DM and generalized BTBR method well correlated.

The agreement at the initial penalty stiffness and the shape of the cohesive law determined by both methods is excellent for all the tested specimens; however there is a shift in some of the cohesive laws that may be due to the inaccuracy in the determination of the crack tip shear displacement by the generalized BTBR approach. It also noticeable that the fracture toughness predicted by generalized BTBR method is slightly higher for all the tested configurations.

It should be noted that results obtained by the original BTBR method neglecting the effect of the adhesive layer thickness reveals high inaccuracies on the predicted initial penalty stiffness and the maximum stresses. Those errors increase with the adhesive thickness versus adherend thickness ratio, being higher for the A1T1 and A2T2 specimen configurations.

On the other hand, it is noticeable in **Figs. 10-16** that, for all specimens except A2T1 09 and A3T1, the tractions in the cohesive laws tend to a non-zero steady value, preventing the corresponding *J*-*Δ* curves from reaching the plateau, an effect that is also noticed in the plateau response exhibited by those specimens in the load-displacement curves shown in **Fig.9**. This behavior denotes the proximity of the fracture process zone to the local compression at the load application point which hinders the complete development of the FPZ.

According to the numerical results, this effect could have been avoided by the eccentric configuration of the ENF test, which provides a wider path for the FPZ development without the need for drastic changes to the test configuration just moving the load application point. In any case, it would be necessary to control both the maximum shear stress and the maximum bending stresses to ensure the elastic behavior of the un-cracked region.

5.2.2. Extrapolation procedure

Once validated the generalized BTBR model and consequently the novel expressions derived for the Compliance, *J*-Integral and Crack Tip Shear displacement including the bond line thickness effect, the suitability of the extrapolation procedure proposed in the present study is analyzed in this section.

Applying the flow chart presented in **Fig. 4** to the experimental data corresponding to the ENF tests of specimens A1T1-09, A2T1-09, A3T1 and A2T2-04, J_0-Δ_0 and Δ_0-C_0 curves corresponding to each specimen are shown in **Fig. 17** and **Fig. 18**, respectively.

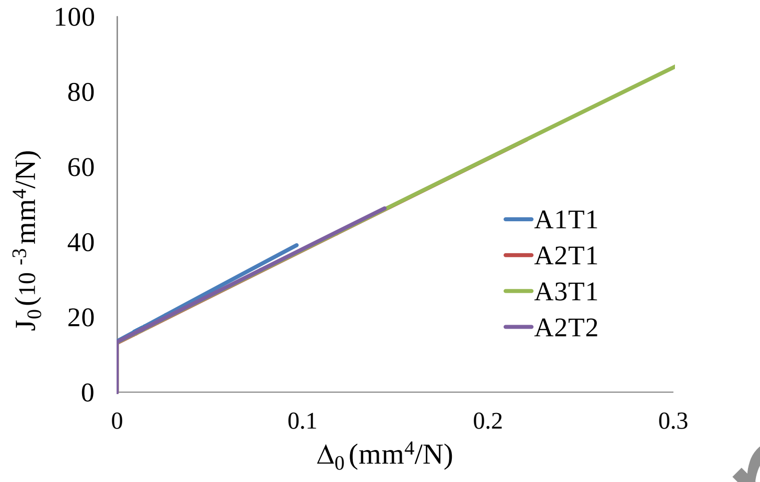

Figure 17. J_0-Δ_0 curves A1T1-09, A2T1-09, A3T1 and A2T2-04.

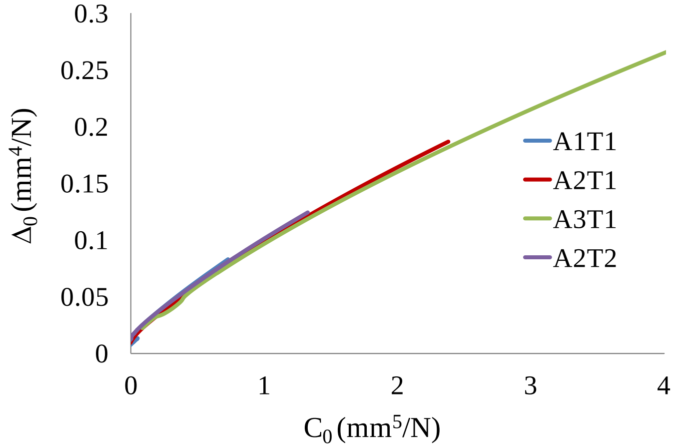

Figure 18. Δ_0-C_0 curves corresponding to A1T1-09, A2T1-09, A3T1 and A2T2-04.

According to **Fig. 17 and Fig. 18**, it can be validated experimentally that J_0-Δ_0 and Δ_0-C_0 curves are invariant for a given material system and test configuration.

Therefore, if J_0-Δ_0 and Δ_0-C_0 relationships are obtained from a single specimen test and fitted to Eq. (14) and Eq. (15), being the input data the P-δ curve, J and Δ_t and according to the flow chart shown in **Fig. 4**, the Cohesive Law for different adherent and adhesive thicknesses of the same material system and test configuration can be extrapolated according the flow diagram presented in **Fig. 5,** being the input data de load-displacement curve and the cross sectional dimensions.

Thus, extracting the J_0-Δ_0 and Δ_0-C_0 curves form specimen A1T1 data, from the flow chart in **Fig. 4** and applying the procedure presented in **Fig. 5**, the Cohesive Law for the specimens A1T1-09, A2T1-09, A3T1 and A2T2-04 are show on in **Fig. 19** compared with the cohesive laws determined by the generalized BTBR method and DM method.

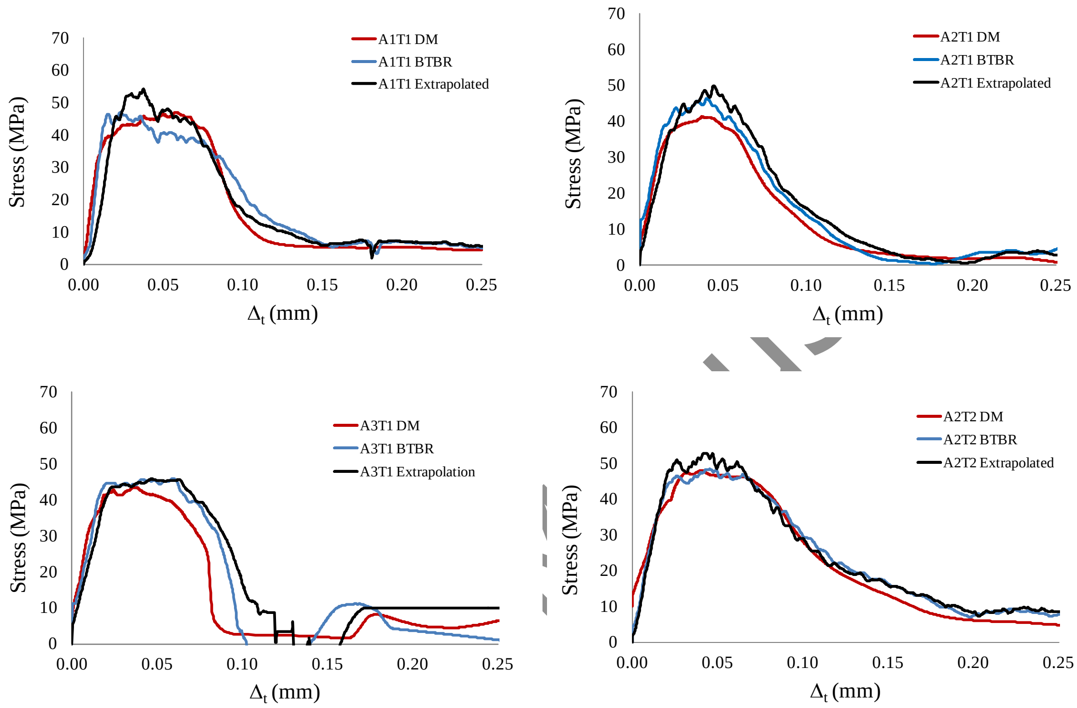

Figure 19. Extrapolated Cohesive Laws for A1T1, A2T1, A3T1 and A2T2 specimens.

According to **Fig. 19**, the extrapolation procedure presented above enables to estimate the cohesive law for a given material system varying the adhesive and adherent thicknesses by processing only the load-displacement curve, calibrating previously the J_0-Δ_0 and Δ_0-C_0 curves using a single specimen test data.

6. SENSITIVITY ANALYSIS

In this section, a Monte Carlo Method based sensitivity analysis is carried out to describe the impact of the input parameter uncertainties in the estimation of the fracture properties of the adhesive bond J, Δ_t and τ obtained by means of the proposed BTBR method. In the present study we focus on the variability of the applied load, the initial specimen dimensions and the mechanical properties of the adherends.

Each variable is sampled using the corresponding probability density function. The elastic properties are assumed to follow a normal distribution and are sampled by a *Normal Distribution*$^{-1}$ *(mean; SD: standard deviation)* function, while the load cell, caliper and micrometer probability density functions are assumed to follow a uniform distribution and are sampled by *Uniform Distribution*$^{-1}$ *(mean; bound)*.

The used testing data and corresponding uncertainties are given in Table 5:

Table 5. Mean values and uncertainties of the applied load, the initial specimen dimensions and the mechanical properties of the adherends.

Test Data	Units	Bounds
P	N	± 0.005P
$2L$	mm	± 0.2
a_i	mm	± 0.2
b	mm	± 0.03
$2h$	mm	± 0.002

Test Data	Units	SD
E_f	MPa	0.05 E_f
G	MPa	0.05 G

The uncertainty bounds reported in Table 5 correspond to typical values of uncertainty of the measuring devices or typical values of dispersion of results in the elastic properties.

At each iteration, random values of J, Δ_t and τ are generated replacing the sampled input variables in the **BTBR method** following the procedure presented in **Section 4.3**.

After 100 iterations, the mean value and standard uncertainty associated to the J, Δ_t and τ are presented in **Fig 20** assuming they follow a normal distribution.

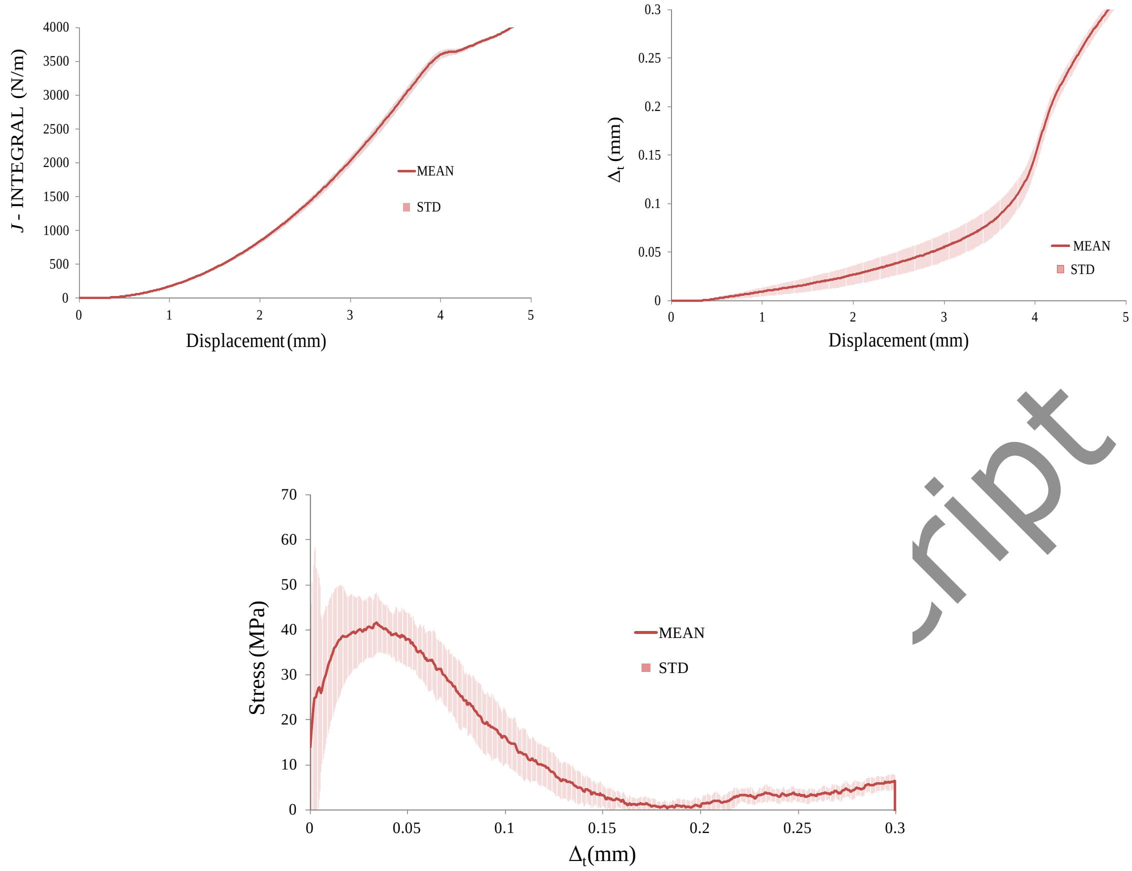

Figure 20. Mean value and standard uncertainty of the fracture toughness, crack tip shear displacement and cohesive law, respectively, using the proposed BTBR method, for the A2T109 specimen

If the uncertainties (CV%) associated to the facture toughness and the crack tip shear displacement are compared (Fig 21), it is noticeable that the uncertainty corresponding to *J*-Integral is much lower than that of Δ_t. It can be stated too, that at the initial states of the test, where the crack tip shear displacement is a small quantity (Δ_t < 5 micras), the uncertainty tends to infinity, which makes this interval not useful for the determination of the cohesive law.

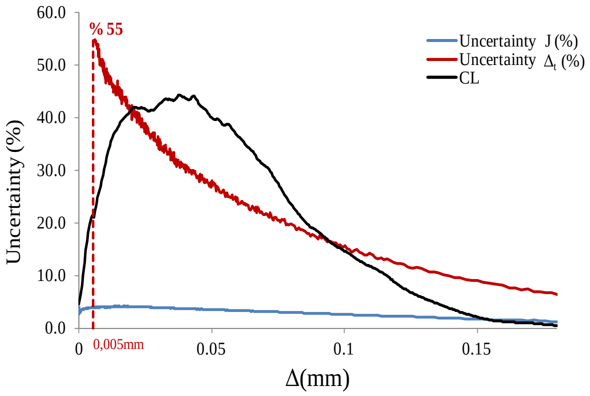

Figure 21. Uncertainties (CV%) associated to the facture toughness and the crack tip shear displacement, for the A2T109 specimen

As the cohesive stresses are determined according to Eq (2) by numerical differentiation, it can be concluded that the main source of the uncertainty corresponding to the cohesive stresses comes from the crack tip shear displacement.

7. SUMMARY AND CONCLUSIONS

A novel extrapolation method to predict the mode II cohesive laws of bonded joints is presented that enables to estimate the mode II cohesive laws for a wide range of adhesive to adherend ratio of a given material system and test configuration.

For that purpose, improved expressions for the compliance, *J* Integral and the crack tip shear displacement are derived generalizing and extending the original BTBR method for the EENF test and to take into account the effect of the adhesive layer thickness, when it is not negligible in comparison with the adherend thickness.

Assuming that every effect associated to the damage is included in the equivalent crack length, new factorized expressions for the Compliance (C_0), *J*- Integral (J_0) and crack tip shear displacement (Δ_0) are defined and based on the invariant relations between J_0-Δ_0 and Δ_0- C_0 for a given material system and test configuration, an extrapolation procedure is presented which enables to estimate the mode II cohesive laws for a wide range of adhesive to adherend ratio of a given material system by processing only the load –displacement curve.

The advantages of the Eccentric ENF test configuration due to the extended crack propagation path and the suitability of the proposed new analytical expression and data reduction scheme to extract the cohesive laws in an eccentric test configuration have been numerically confirmed. On the other hand, the validity of the developed compliance, *J*- Integral and the crack tip shear displacement expressions have been verified experimentally for four different specimen configurations, combining two adhesive thicknesses and three adherend thicknesses, by comparing results obtained by the original and generalized BTBR method with those obtained by the Direct Method. Results reveal the need of including the influence of the thickness of the adhesive line in the data reduction scheme to obtain accurate results, especially in those cases where the adhesive thickness versus adherend thickness ratio is higher.

Moreover, the suitability of the extrapolation procedure and the precision of the extracted cohesive laws have been confirmed experimentally by comparing predicted cohesive laws with results obtained by the Direct Method.

Finally, a sensitivity analysis has been performed to evaluate the reliability of the proposed BTBR method. Applying a Monte Carlo simulation, the standard uncertainties corresponding to the fracture toughness, the crack tip shear displacement and the cohesive law have been estimated. It has been concluded that the main uncertainty source on the determination of the cohesive law is the crack tip shear displacement.

ACKNOWLEDGMENTS

Financial support of the University of the Basque Country (UPV/EHU) in the Research Group GIU 16/51 “Mechanics of Materials” is acknowledged. The authors would like to acknowledge the support of the Spanish Government though the Ministerio de Economia y Competitividad under the contract RTI2018-099373-B-I00.

APPENDIX A

The displacement of the loading point is determined applying the Engesser–Castigliano’s theorem [36], which in the case of shear and bending is given by

$$\delta_i = \left[\frac{\partial U^*}{\partial F_i}\right]_a = \int \frac{M}{E_f I}\frac{\partial M}{\partial F_i}dx + \int \frac{6}{5}\frac{Q}{G_{13}A}\frac{\partial Q}{\partial F_i}dx \quad \text{(A1)}$$

being the derivatives obtained applying a vertical unit load at the middle point of the specimen, the middle point displacement can be expressed as:

$$\delta = P(\Omega_1 {a_e}^3 + \Omega_2 a_e + \Omega_3) \quad \text{(A1)}$$

where a_e is equivalent crack length and Ω_1, Ω_2 and Ω_3 parameters are :

$$\begin{aligned}
\Omega_1 &= \frac{1}{6E_f I_0}(1-\alpha)^2 - \frac{1}{3E_f I}(1-\alpha)^2 \\
\Omega_2 &= \frac{6}{5}\left[\frac{1}{2G_{13}A_0}(1-\alpha)^2 - \frac{1}{G_{13}A}(1-\alpha)^2\right] \\
\Omega_3 &= \frac{(2L)^3}{3E_f I}[(1-\alpha)^2\alpha^3 + (1-\alpha)^3(\alpha)^2] + \frac{6(2L)}{5G_{13}A}[(1-\alpha)^2\alpha + (1-\alpha)(\alpha)^2]
\end{aligned} \quad \text{(A2)}$$

Designing as $\alpha = d/2L$ the shape factor accounting for the eccentricity of the EENF test in the deformed configuration.

Thus, the compliance at the load application point can be expressed as:

$$\begin{aligned}
C = \frac{\delta}{P} &= \frac{(1-\alpha)^2}{3E_f}\left[\frac{1}{2I_0} - \frac{1}{I}\right]{a_e}^3 + \frac{(1-\alpha)^2\alpha^2}{3E_f I}(2L)^3 + \frac{6}{5}\frac{(1-\alpha)^2}{G_{13}}\left[\frac{1}{2A_0} - \frac{1}{A}\right]a_e \\
&\quad + \frac{6}{5}\frac{(1-\alpha)\alpha}{G_{13}A}(2L)
\end{aligned} \quad \text{(A3)}$$

The second moment of areas and the cross sectional areas are

$$I_0 = \frac{1}{12}w\left[\frac{(2h-t)}{2}\right]^3 \qquad A_0 = w\left[\frac{(2h-t)}{2}\right]$$
$$I = \frac{1}{12}w[2h]^3 \qquad A = w[2h] \quad \text{(A4)}$$

Defining $\beta = t/2h$ as the adhesive to adherent thickness ratio:

$$\left[\frac{1}{2I_0} - \frac{1}{I}\right] = \frac{1}{I}\left[\frac{4-(1-\beta)^3}{(1-\beta)^3}\right] = \frac{1}{I}\left[\frac{1}{\chi}\right] \qquad \left[\frac{1}{2A_0} - \frac{1}{A}\right] = \frac{1}{A}\left[\frac{\beta}{1-\beta}\right] \quad \text{(A5)}$$

Where χ factor can be computed as:

$$\chi = \frac{(1-\beta)^3}{4-(1-\beta)^3} \quad \text{(A6)}$$

Rewriting Eq (A4) :

$$C=\frac{12(1-\alpha)^2}{E_f w(2h)^3}\left[\frac{1}{\chi}\frac{{a_e}^3}{3}+\alpha^2\frac{(2L)^3}{3}\right]+\frac{6}{5}\frac{(1-\alpha)}{G_{13}w(2h)}\left[(1-\alpha)\left[\frac{\beta}{1-\beta}\right]a_e+\alpha(2L)\right] \qquad \text{(A7)}$$

According to Eq (A7) an initial compliance C_{ini} can be defined as the compliance corresponding to the initial equivalent crack length a_{ie}, consequently C-C_{ini} can be determined as

$$C-C_{ini}=\frac{4(1-\alpha)^2}{E_f w(2h)^3}\frac{1}{\chi}\left[\ {a_e}^3-{a_{ie}}^3\right]+\frac{6}{5}\frac{(1-\alpha)^2}{G_{13}w(2h)}\left[\frac{\beta}{1-\beta}\right][a_e-a_{ie}] \qquad \text{(A8)}$$

Rewriting the above expression, it yields to:

$$C-C_{ini}=\frac{4(1-\alpha)^2}{E_f w(2h)^3}\frac{1}{\chi}\left[\ {a_e}^3-{a_{ie}}^3\right]\left[1+\frac{3}{10}\frac{E_f}{G_{13}}(2\mathrm{h})^2\chi\left[\frac{\beta}{1-\beta}\right]\frac{[a_e-a_{ie}]}{[{a_e}^3-{a_{ie}}^3]}\right] \qquad \text{A9}$$

where $\frac{3}{10}\frac{E_f}{G_{13}}(2\mathrm{h})^2\chi\left[\frac{\beta}{1-\beta}\right]\frac{[a_e-a_{ie}]}{[{a_e}^3-{a_{ie}}^3]}$ is negligible for all the tested configurations, C-C_{ini} can be expressed as:

$$C-C_{ini}=\frac{4(1-\alpha)^2}{E_f w(2h)^3}\frac{1}{\chi}\left[\ {a_e}^3-{a_{ie}}^3\right] \qquad \text{A10}$$

REFERENCES

[1] Duarte AP, Coelho JF, Bordalo JC, Cidade MT, Gil MH. Surgical adhesive: Systematic review of the main types and development forecast. Prog. Polym. Sci 2011; 37 (8): 1031–1050.

[2] Oehlers DJ. Development of design rules for retrofitting by adhesive bonding or bolting either FRP or steel plates to RC beams or slabs in bridges and buildings. Compos. Part A – Appl. S 2001;32: 1345–1355.

[3] Li Y, Wong CP. Recent advances of conductive adhesives as a lead-free alternative in electronic packaging: materials, processing, reliability and applications. Mater. Sci. Eng 2006; 51 (1–3): 1–35.

[4] Loven WE. Structural bonding of composites in the transportation market. Reinforced Plastics 1999; 43 (6): 40–43.

[5] Higgins A. Adhesive bonding of aircraft structures. Int J Adhes Adhes 2000; 20: 367–376.

[6] Barnes TA, Pashby IR. Joining techniques for aluminium spaceframes used in automobiles. J Mater Process Technol 2000; 99: 72-79.

[7] Alfredsson KS, Högberg JL. Energy release rate and mode-mixity of adhesive joint specimens. Int J Fract 2007;144: 267–283.

[8] Taib A, Boukhili R, Achiou S, Gordon S, Boukehili H. Bonded joints with composite adherends. Part I. Effect of specimen configuration, adhesive thickness, spew fillet and adherend stiffness on fracture. Int J Adhes Adhes 2006; 26 (4): 226–236.

[9] Fernando M, Harjoprayitbi WW, Kinloch AJ. A fracture mechanics study of the influence

of moisture on the fatigue behaviour of adhesively bonded aluminium-alloy joints. Int J Adhes Adhes 1996; 16 (2): 113-119.
[10] Jumel J, Budzik MK, Ben Salem N, Shanahan MER. Instrumented End Notches Flexure-Crack propagation an process zone monitoring. Part I Modelling and Analysis. Int J Sol Str 2013; 50 (2) : 297-309.
[11] Katsiropoulos ChV, Chamos AN, Tserpes KI, Pantelakis SpG. Fracture toughness and shear behavior of composite bonded joints based on a novel aerospace adhesive. Compos Part B- Eng 2012; 43 (2): 240–248.
[12] Jumel J, Budzik MK, Ben Salem N, Shanahan MER. Instrumented End Notches Flexure-Crack propagation an process zone monitoring. Part II: Data reduction and experimental. Int J Sol Str 2013; 50 (2) : 310-319.
[13] Barenblatt GI. Mathematical Theory of Equilibrium Cracks in Brittle Fracture. Adv Appl Mech 1962; 7: 55-129.
[14] Dugdale DS. Yielding of steel sheets containing slits. Mech Phys Solids 1960; 8: 100–104.
[15] Park K, Paulino G. Cohesive zone models: a critical review of traction separation relationships across fracture surfaces. Appl Mech Rev 2011; 64 (6).
[16] Sarrado C, Turon A, Costa J, Renart J. An experimental analysis of the fracture behavior of composite bonded joints in terms of cohesive laws. Compos Part A 2016; 90: 234–42.
[17] Dourado N, de Moura MFSF, de Morais AB, Pereira AB. Bilinear approximations to the mode II delamination cohesive law using an inverse method. Mech Mater 2012; 49: 42-50.
[18] de Morais AB, Pereira AB, de Moura MFSF, Silva FGA, Dourado N. Bilinear approximations to the mixed-mode I–II delamination cohesive law using an inverse method. Compos Struct 2015;122: 361-366.
[19] de Morais AB. Evaluation of a trilinear traction-separation law for mode II delaminationusing the effective crack method. Compos Part A 2019; 121: 74-83
[20] Xu Y, Li X, Wang X, Liang L. Inverse parameter identification of cohesive zone model for simulating mixed-mode crack propagation. Inter J Sol Struct 2014; 51: 2400-2410.
[21] Xu Y, Guo Y, Liang L, Liu Y, Wang X. A unified cohesive zone model for simulating adhesive failure of composite structures and its parameter identification. Compos Struct 2017;182:555–65.
[22] Jensen SM, Martos MJ, Lindgaard E, Bak BLV. Inverse parameter identification of n-segmented multilinear cohesive laws using parametric finite element modeling. Compos Struct 2019; 225: 111074
[23] Silva FGA, Morais JJL, Dourado N, Xavier J, Pereira FAM, Moura MFSF. Determination of cohesive laws in wood bonded joints under mode II loading using the ENF test. Int J Adhes Adhes 2014; 51; 54-61.
[24] S. Abdel Monsef, M. Pérez-Galmés, J. Renart, A. Turon, P. Maimí The influence of mode II test configuration on the cohesive law of bonded joints. Compos Struct 2020; 234: 111689.
[25] Leffler K, Alfredsson KS, Stigh U. Shear behaviour of adhesive layers. Int J Sol Str 2007; 44: 530- 45.
[26] Alfredsson KS, Biel A, Salimi S. Shear testing of thick adhesive layers using the ENF-specimen. Int J Adhes Adhes 2015; 62 :130-8.
[27] Carlberger T, Stigh U. Influence of Layer Thickness on Cohesive Properties of an Epoxy-Based Adhesive—An Experimental Study. J Adhes 2010; 86: 816-35.
[28] Biel A, Stigh U. Comparison of J-integral methods to experimentally determine cohesive laws in shear for adhesives. International Journal of Adhesion and Adhesives, 94, 64-75.
[29] Svensson D, Alfredsson KS, Biel A, Stigh U. Measurement of traction cohesive laws for interlaminar failure of CFRP. Compos Sci Technol 2014; 100: 53–62.
[30] Stigh U, Alfredsson KS, Biel A. Measurement of cohesive laws and related problems, in:

IMECE 2009: Proceedings of the ASME International Mechanical Engineering Congress and Exposition 2009; 11: 293-298.
[31] Fernandes RMRP, Chousal JAG, de Moura MFSF, Xavier J. Determination of cohesive laws of composite bonded joints under mode II loading. Compos B Eng 2013; 52: 269–74.
[32] Morais AB. Determination of the shear traction-separation law of adhesive layers using the end-notched flexure specimen Eng Fract Mech 2020:235; 107199;
[33] Arrese A, Insausti N, Mujika F, Perez-Galmés M, Renart J. A novel experimental procedure to determine the cohesive law in ENF tests. Compos Sci Technol 2018; 170: 42-50.
[34] Rice JR. A path independent integral and the approximate analysis of strain concentration by notches and cracks. J Appl Mech 1968; 35: 379–86.
[35] Sorensen BF, Jacobsen TK. Determination of traction cohesive laws by the J integral approach. Eng. Fract. Mech 2003;70: 1841–1858.
[36] Oden JT, Ripperger EA. Mechanics of elastic structures. 1981.
[37] A. Arrese, N. Carbajal, G. Vargas, F. Mujika. A new method for determining mode II R-curve by the End-Notched flexure test. Eng. Fract. Mech 2010; 77: 77-20.
[38] Arrese A, Boyano A, de Gracia J, Mujika F. A novel procedure to determine the cohesive law in DCB tests. Compos Sci. Technol 2017; 152:76-84.
[39] Yoshihara H. Mode II fracture mechanics properties of solid Wood measured bu the three-point eccentric end-notched flexure test. Eng. Fract. Mech 2015; 141: 140-151.
[40] Marín L, Trias D, Badalló P, Rus G, Mayugo J. Optimization of composite stiffened panels under mechanical and hygrothermal loads using neural networks and genetic algorithms. Compos Struct 2012; 94: 3321–3326.
[41] Marín L, Gonzalez EV,Maimí P, Trias D, Camanho PP.Hygrothermal effects on the translaminar fracture toughness of cross-ply carbon/epoxy laminates: Failure mechanisms. Compos Sci. Technol 2016; 122:130-139.
[42] Sarrado C, Leone FA, Turon A. Finite-thickness cohesive elements for modeling thick adhesives. Eng. Fract. Mech 2016; 168: 105–113.
[43] AITM 1.0006: Determination of interlaminar fracture toughness energy. Mode II Airbus Industrie Test Method 1994; 2.
[44] Sorensen BF. Cohesive law and notch sensitivity of adhesive joints. Acta Mater 2002; 70: 1053–1061.
[45] Furtadoa C, Arteiroa A, Bessac MA,.Wardled BL, Camanhoa PP. Prediction of size effects in open-hole laminates using only the Young's modulus, the strength, and the -curve of the 0° ply. Compos Part 2017; 101; 306-317.